# Improving a BEM Yaw Model Based on NewMexico Experimental Data and Vortex/CFD Simulations

**F. BLONDEL[a], G. FERRER[a], M. CATHELAIN[a], D. TEIXEIRA[a]**

a. IFP Energies Nouvelles, 92500 Rueil-Malmaison, France, frederic.blondel@ifpen.fr.

## Résumé :

*Les travaux présentés ici ont pour but d'évaluer la capacité de différents modèles à reproduire le sillage ainsi que les efforts sur les pales d'une éolienne testée en soufflerie dans le cadre du projet MexNext (IEA Wind), et améliorer un modèle BEM (Blade Element Momentum) par l'analyse des résultats. Deux solveurs développés en interne à IFPEN (AeroDeeP, CASTOR), basés sur les méthodes BEM (Blade Element Momentum) et vortex ainsi qu'un modèle CFD-AL (Computational Fluid Dynamics - Actuator Line) open-source, SOWFA, basé sur l'outil OpenFOAM ont été mis en œuvre. Les principaux résultats sont donnés ci-après : la BEM permet d'obtenir des résultats proches des méthodes "avancées", même pour le cas en dérapage. Pour ce faire, un nouveau modèle a été introduit. Bien que les essais ne soient pas parfaitement reproduits, ce modèle simple améliore nettement les résultats. Dans le sillage, la méthode vortex permet d'obtenir des résultats très proches des mesures du fait de la faible diffusion du modèle.*

## Abstract:

*The aim of the work presented here is to evaluate the capacity of three models to reproduce the blade loads and near wake velocities of a wind turbine, tested in a wind tunnel during the IEA Wind MexNext project ant to improve a Blade Element Momentum (BEM) model based on the analysis of the results. Two in-house solvers (AeroDeeP, CASTOR), based on BEM and vortex methods, are compared to an open-source CFD Actuator Line solver (CFD-AL) named SOWFA, based on the OpenFOAM toolbox. The main conclusions are given below: the BEM model reach the accuracy of other numerical methods for blade loads, even in yawed conditions. To this end, a new simple model has been introduced. Although the results do not compare perfectly with experimental data, a substantial improvement has been obtained. Wake velocities are well predicted by the vortex solver, thanks to the low diffusion of the methods.*

**Keywords: wind turbines, aerodynamics, yaw, BEM, Vortex, CFD, SOWFA.**

## 1 Introduction

Nowadays, most of the wind turbine design software rely on Blade Element Momentum models [12]. These methods are based on strong hypotheses, partially overcome through analytical corrections,

introducing empiricism in the model. The reliability of the model is then questionable, especially in the framework of large fixed and floating offshore wind turbines, which tend to become larger and larger, reaching 10MW or more [3]. Thus, improvement and validation are crucial. On the other side, more physical models, such as the vortex or CFD-AL models (CFD using an Actuator Line representation of the wind turbine blades), are being increasingly used. Both are based, with their own hypothesis, on the modelling of the wake and the evaluation of the impact of the wake on blade loads. The wake being fully modelled, these models require less analytical corrections. Validation results have already been presented by Blondel et al. [1], focusing mostly on blade loads. Here, the benchmark is extended to the wake velocities, including a CFD-AL model of the wind turbine. The aim of this paper is to compare the solvers against up-to-date wind tunnel experiments and improve the BEM model based on the analysis of the simulations results experimental measurements. As shown in [1], BEM models are not accurate enough in yawed cases. Here, a new model improving BEM predictions is proposed. The final objective is to adopt a tool that could be coupled with the aero-servo-hydro-elastic solver DeepLines Wind™ [9], in order to get accurate results with low computational costs when dealing with complex configurations, such as floating wind turbines, HAWTs (Horizontal Axis Wind Turbines), of tandem wind turbines concepts, which gain attention recently.

# 2 Solvers description

## 2.1 AeroDeeP: BEM based aerodynamic library

AeroDeeP is based on the widely used Glauert's Blade Element Momentum method [5], inspired from the Rankine-Froude theory, using two-dimensional airfoil characteristics to evaluate the forces at each blade element. Induction factors, which represent the momentum loss due to the presence of the rotor, are computed in both axial and tangential directions along the blade span. In order to overcome the major limitations of the classical BEM theory, corrections have been implemented to account for hub and tip losses, turbulent wake state, tower shadowing, dynamic inflow (i.e. unsteady BEM), dynamic stall, as well as yawed rotor configurations. In the present, Prandtl tip losses are used and the turbulent wake state model is based on the recent works by Ning et al. [10]. The stall model will be introduced in 2.1.1. For all the presented calculations, 35 elements per blade have been used, and 20 rotations of the wind turbine have been performed, using an azimuthal step of $10°$. The resulting computational time is below 3 seconds.

### 2.1.1 Modification of the Øye dynamic stall model

A first approach for modelling the dynamic stall phenomenon is the Øye model (see [11]). The stall is simulated using a single ordinary differential equation representing the time lag of the separation point displacement. Øye defines a dynamic ($f_d$) and a static ($f$) attachment degree function, representing the position of the separation point on the suction side of the airfoil. The relation between the static and the dynamic functions simply writes:

$$\frac{df_d}{dt} = \frac{(f - f_d)}{\tau}, \tag{1}$$

$\tau$ is defined by Øye as $\tau = A_1 c/V$, $A_1$ being a constant usually set to $A_1 = 4$, $c$ the airfoil chord, and $V$ the norm of the airfoil relative velocity. Once the static attachment function is determined,

Equation 1 can be numerically integrated. To do so, one first needs to define the lift coefficient under fully attached and fully separated flow conditions ($C_{l,fa}$ and $C_{l,fs}$, respectively). The actual lift coefficient, $C_l$, given by the airfoil polar, is nothing but a ponderation of those two coefficients and the attachment degree function. Thus, the function $f$ can be found inverting the following relation:

$$C_l = fC_{l,fa} + (1-f)C_{l,fs}. \tag{2}$$

The lift under fully attached flow conditions is based on the lift curve slope around $\alpha_0$:

$$C_{l,fa} = \left.\frac{\partial C_l}{\partial \alpha}\right|_{\alpha_0} (\alpha - \alpha_0), \tag{3}$$

$\alpha$ being the angle of attack and $\alpha_0$ being the angle of attack where the lift is equal to zero. The determination of the fully separated lift coefficient is a bit more tricky, and this is where we differ from the original model. In the current implementation, we use a rather common approach (see [7]) based on the Kirchhoff flow theory (Equation 4) to determine a first attachment degree function value, rather than interpolating the lift curve slope near the zero lift angle of attack and the full stall angle of attack, as suggested by Øye:

$$C_l \simeq \left(\frac{1+\sqrt{f}}{2}\right)^2 C_{l,fa}. \tag{4}$$

Equation 4 is inverted, taking care of possible singularities, and then the value of $f$ is used to determine the fully separated lift coefficient based on Equation 2. Finally, the dynamic lift coefficient computed using Equation 5, which is nothing but Equation 2 using the dynamic attachment degree function:

$$C_{l,dyn} = f_d C_{l,fa}(\alpha) + (1-f_d)C_{l,fs}(\alpha). \tag{5}$$

As shown in Equation 5, the Øye model only describes the dynamic lift evolution. Dynamic drag and moment coefficient are thus considered to be equal to their static counterparts for a given angle of attack.

### 2.1.2 A new yaw model

A yaw model has been specially developed for the BEM method. This model can be seen as a compromise between the standard Glauert model [5], which is not able to represent the root vortex effect, and the more recent yaw model by Schepers [14], which depends on many empirical constants. In the model, only two phase angles are defined: the first one for the root vortex effect and the second for the tip vortex effect. Based on the analysis of vortex solver results, it has been noticed that the phase of the normal force due to the tip vortex and the phase shift due to the root vortex were almost constant along the span: only the intensity of the normal force fluctuations is changing, as shown in Appendix A, Figures 8 and 9, the phenomenon being mostly visible at high yaw angles (Figure 9). This will be detailed in section 4.2. Thus, we simply combined two identical models, the first being related to the tip vortex influence and the second to the root vortex influence. Then, a linearly increasing function is used to increase the influence of the tip vortex with blade span, and a linearly decreasing function is used to decrease the influence of the root vortex with blade span. One can notice that the correction is directly applied to the local values of the induction factor ($a = 1 - u/U_\infty$).

No corrections are applied to the tangential induction factor. Finally, our model reads:

$$a_{yaw} = a\left[1 + k_1(r/R)\frac{r}{R}\tan(\chi/2)\sin(\psi+\phi_1) + k_2(r/R)\left(1-\frac{r}{R}\right)\tan(\chi/2)\sin(\psi+\phi_2)\right], \quad (6)$$

with $a$ the local element axial induction factor, $\psi$ the blade azimuth angle and $\chi$ the wake skew angle, defined as $\chi = \Psi(0.6a_{rotor}+1)$, with $\Psi$ the yaw angle, and $a_{rotor}$ the rotor averaged axial induction factor. After some calibration, phase angles and linear functions have been defined as:

$$\phi_1 = -\pi/9, \qquad \phi_2 = \pi, \qquad A_0 = 0.35, \quad (7)$$

$$k_1(r/R) = (1-A_0) + A_0\frac{r-r_{hub}}{R-r_{hub}} \qquad k_2(r/R) = 1 - A_0\frac{r-r_{hub}}{R-r_{hub}}. \quad (8)$$

## 2.2 CASTOR: GPU based lifting-line free-wake model

CASTOR (Code Aerodynamique pour la Simulation de Turbines OffshoRe) is a free-wake vortex filament lifting-line solver based on the generalized Prandtl lifting-line theory (see [15], [8]). Various flow effects such as turbulent wake state, dynamic inflow, hub and tip losses, as well as skewed rotor configurations are inherently taken into account. Similarly to the BEM method, CASTOR is based on airfoil polars, so that blade surfaces do not have to be modelled. In order to reduce the computational costs, CASTOR is based on an hybrid OpenMP / GPU implementation, thereby reducing the computational times up to two orders of magnitude when compared to sequential CPU implementations. The modified Øye model introduced in Section 2.1.1 as well as Beddoes-Leishman modified Risø stall model [7] have been implemented. For all the presented calculations, the modified Øye model is used, with 35 elements per blade, and 20 rotations of the wind turbine have been performed, together with an azimuthal step of $10°$, which is commonly used. The resulting computational time is around 38 minutes (physical time) on an NVIDIA Tesla K40m Graphical Processing Unit. Such a calculation would take days on a single CPU. Here, efforts have been made to reach an highly converged state. For standard calculations, 10 rotations are sufficient, and the computational time is reduced to approximatly 7 minutes (physical time).

## 2.3 SOWFA: actuator-line model based on OpenFOAM

The CFD solver used in this study is SOWFA (Simulator for Offshore Wind Farm Applications), an OpenFOAM-based solver developed at the National Renewable Energy Laboratory (NREL), as briefly presented in [4]. The simulations have been computed on a $24D \times 6D \times 6D$ domain and three local refinements (i.e. 3 cylinders of radius $2D$, $1.5D$ and $1D$) on an initial Cartesian mesh ($192 \times 48 \times 48$ grid points) leading to a local spatial discretisation of $0.016D$ near the blade ($\approx 30$ cells per blade) and a final grid size of 24 million cells. The wind is considered as uniform at the inlet of the domain and an “inletOutlet" condition is applied at the outlet. Lateral boundaries are defined as cyclic boundaries and a slip condition is applied at the upper and lower boundaries. The LES (Large Eddy Simulation) has been adopted, with a Smagorinsky eddy viscosity model. The turbine is modelled using the actuator line approach based on the transient solver “pisoFoamTurbine.ALM", thus using airfoil polars. Input values for the ALM such as the number of actuator line elements is set to 64 and the Gaussian width parameter satisfies the criterion $\varepsilon \leq 2\Delta x$. A Glauert correction for the tip loss is selected. The simulation time was 10 seconds with a time step of $2 \times 10^{-4}$ seconds,

ensuring that the tip does not pass through more than one grid cell during the time increment. The resulting computational time is approximatly 8 hours (physical time) on 128 Intel SandyBridge cores for 20 rotor rotations. Regarding the loads and radial traverses, presented results have been averaged over 10 and 5 rotations respectively.

# 3 Experimental data

The NewMexico experiments have been performed in the DNW $9.5 \times 9.5\text{m}^2$ closed walls large low-speed facility test section. A 4.5m diameter three bladed rotor has been used. In the considered cases, the rotor rotates at approximately 424.5rpm, and the pitch angle of the blades is $\theta = -2.3°$. The twisted and tapered blades are based on $DU91\text{-}W2\text{-}250$, $RISO\text{-}A1\text{-}21$ and $NACA64\text{-}418$ airfoils from root to tip. Both blade coning and hub tilt angles are equal to zero. Normal and tangential forces distributions are obtained through the integration of the measured pressures at five radial positions along the blade. A complete description of the experiment can be found in [2]. In all cases presented here, the rated wind velocity ($\approx 15$m/s) has been used.

# 4 Results

## 4.1 Axial flow conditions

First, the solver predictions are compared with experimental data under axial flow conditions. Normal and tangential forces are shown on Figure 1. For all three solvers, a very good agreement is obtained. Main differences are located near the tip. Both the BEM and the CFD-AL solvers are based on the Glauert tip correction. The vortex model does not need such correction. Although the tangential force magnitude is approximately an order of magnitude below the normal forces, the predictions are found to be accurate at this rated wind velocity. The next comparisons deal with the axial PIV traverses.

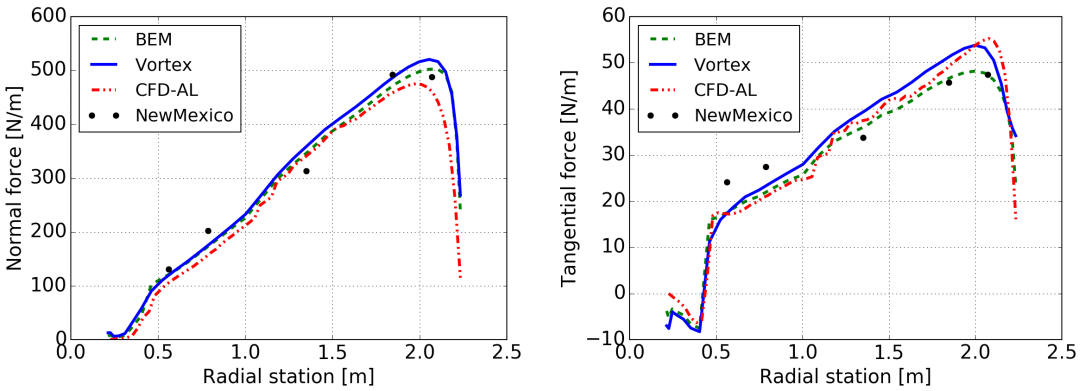


Figure 1: Comparison of normal (left) and tangential (right) forces along the blades.

Measurements are taken at two radius: $r = 0.5$m (inner) and $r = 1.5$m (outer) in the 9 o'clock plane when looking from upstream, and are instantaneous snapshots of the velocity when blade 1 azimuth is 0. The three components of velocity are shown on figure 2, the axial distance to the rotor (located at $x = 0$m) ranges from $-1.0$ rotor diameter to $+1.5$ rotor diameter approximately. For the various velocities, some oscillations appear. These oscillations are due to the root vortex (inner traverse) and

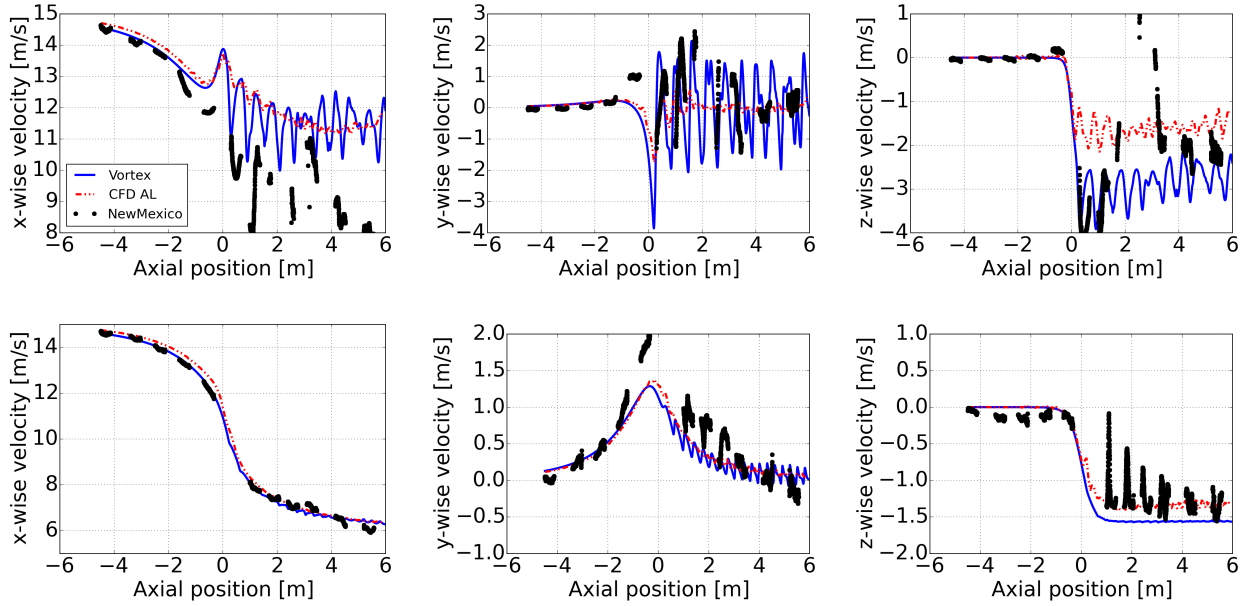


Figure 2: Comparison of instantaneous axial traverse velocities: inner (top) and outer (bottom).

the tip vortex (outer traverse). Agreement is correct near the root, although just in front of the rotor the experimental trends are not followed, which is due to the absence of hub in the simulations (see [13]). Agreement with the experimental data is very good near the tip (outer traverse). The x-wise component of the velocity highlights the flow deceleration due to the presence of the rotor (upwind) but also due to its wake (downstream, positive $x$). Fluctuations of the y-wise and z-wise velocities are also well caught. Only small differences are noticed between the vortex and the CFD-AL solvers: both follow the experimental trends very well. Near the root (inner traverse), oscillations are much

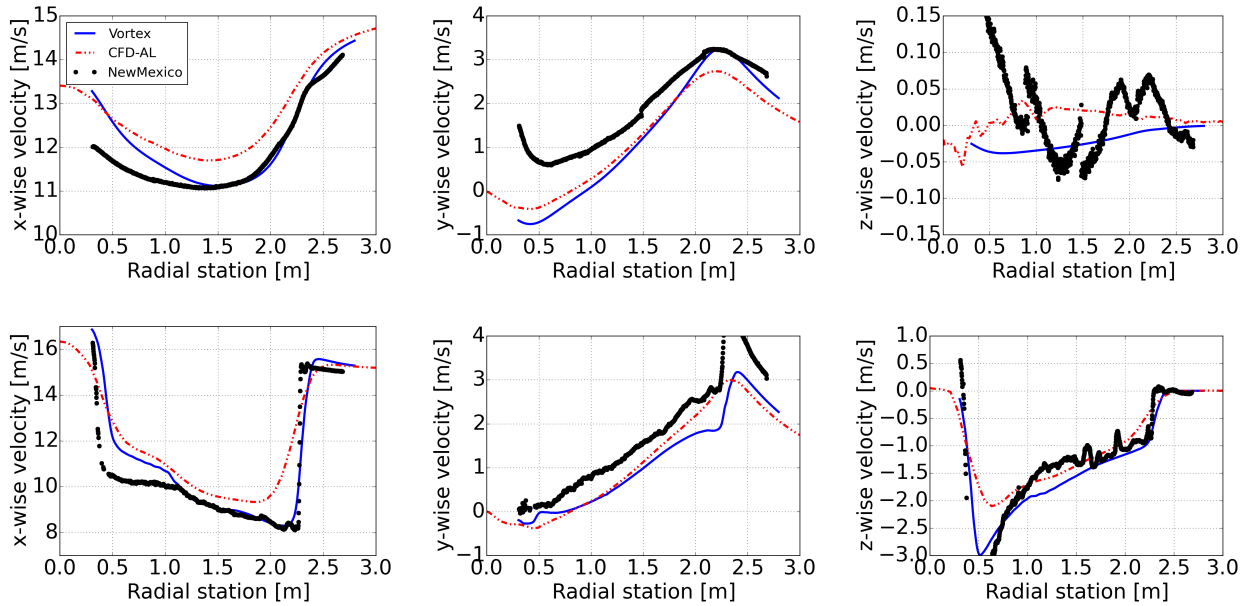


Figure 3: Comparison of radial traverse averaged velocities upstream (top) and downstream (bottom) of the rotor blades.

more pronounced. Although the experimental trends are more or less followed, the large oscillation amplitudes make it difficult to conclude here. One can notice that the oscillations predicted by the CFD-AL are smaller than the one predicted by the vortex solver. The vortex solver predictions seem to be more consistent with the measurements. We also notice that the CFD-AL results are consistent with the recent results presented by Sarmast et al. [13], using a similar CFD-AL model. The next comparison (Figure 3) deals with the radial traverses. The PIV traverses are located in the 9 o'clock plane, upstream $x = -0.3$m and downstream $x = +0.3$m of the rotor, and velocities are averaged over $120°$. Agreement between the measurements and the vortex solver is very good, both upstream and downstream of the rotor. Some deviations are noticed near the root of the blade. Sarmast et al [13] recently analysed this phenomenon and a clear conclusion on the impact of the hub presence was drawn. Yet, the tip vortex effect clearly appears on calculation and measurements at radial station $y = 2.15$m, and is pretty well caught. The CFD-AL results are also in good agreement with experimental data, but the tip vortex is not as sharp as in measurements/vortex calculations. This might be due to a too coarse mesh resolution leading to an excessive diffusion.

## 4.2 Yawed flow conditions

For this second computational case, a rotor yawed by $30°$ is considered. The inflow conditions and rotational velocities are still the same. Blade loads are shown on Figure 13 at three radial stations: near the root (left), at mid-span (center), and near the tip (right). Normal and tangential forces evolution are shown with respect to the azimuth angle. During the wind turbine rotation, the blade perceived a varying relative wind velocity, advancing and retreating with respect to the incoming wind, depending on the azimuth. The advancing and retreating effect induces load fluctuations. It is

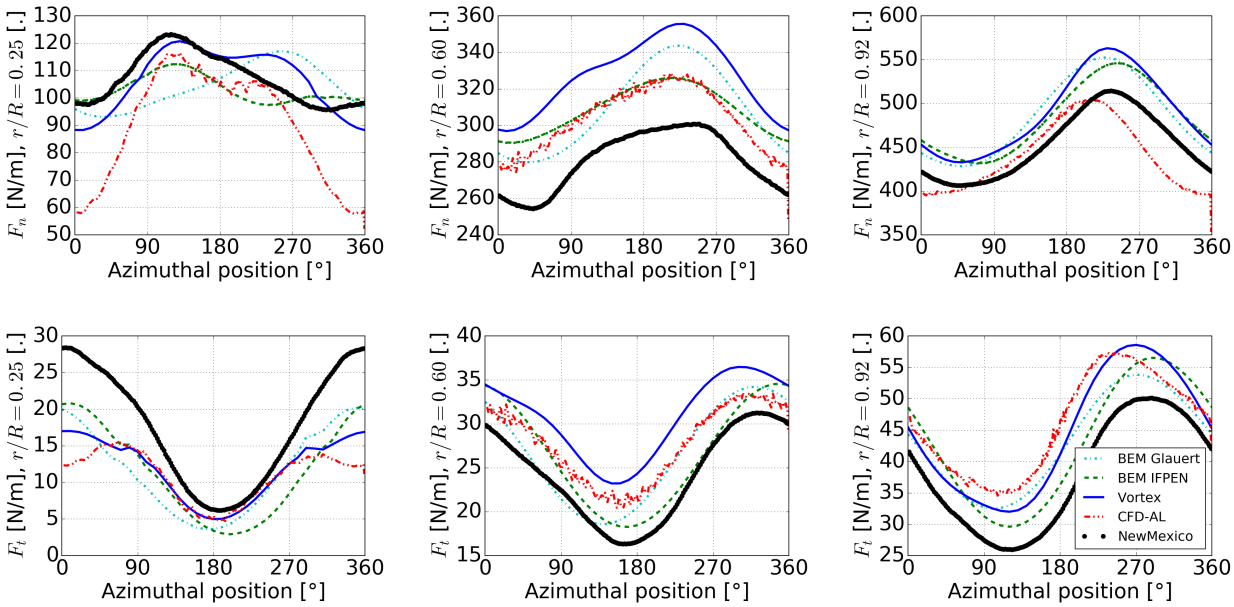


Figure 4: Yawed flow - Normal (up) and tangential (down) forces near the root (left), near mid-span (center) and near the tip (right). $U_\infty \approx 15m/s$, $\Psi \approx 30°$.

noticeable that the maximum of the normal force near the tip and at mid span is located near azimuth $\Psi = 240°$, whereas it is located near $\Psi = 100°$ near the tip (see also figures in Appendix A). It has been proven by Schepers in [14] that this phase shift is due to the presence of the root vortex. As

shown on Figure 4, this phenomenon is well caught by the vortex and the CFD-AL solver, but the standard BEM model with Glauert correction does not predict the phase shift. This is the reason why a new simple yaw model has been derived (see section 2.1.2), referred to as “BEM IFPEN". Although the loads are not perfectly caught, the improvement is clear when compared with the Glauert model, preserving its accuracy near the tip of the blade. One of the main advantage of the presented model when compared to the model by Schepers [14] is the very low number of constants, which makes it more generic: the fit with experimental data might sometimes be less accurate, but the model is much more generic and has been validated on other yaw configurations ($8°$, $15°$, $45°$), wind velocities and other experimental data (such as the UAE database, see [6]), some of them being included in Appendix B. The low magnitudes of the normal and tangential forces near the root of the blade predicted by the CFD-AL solver are due to the absence of stall. Similar trends were observed with the BEM and vortex models without stall. The rest of the blade is not impacted. As for the axial

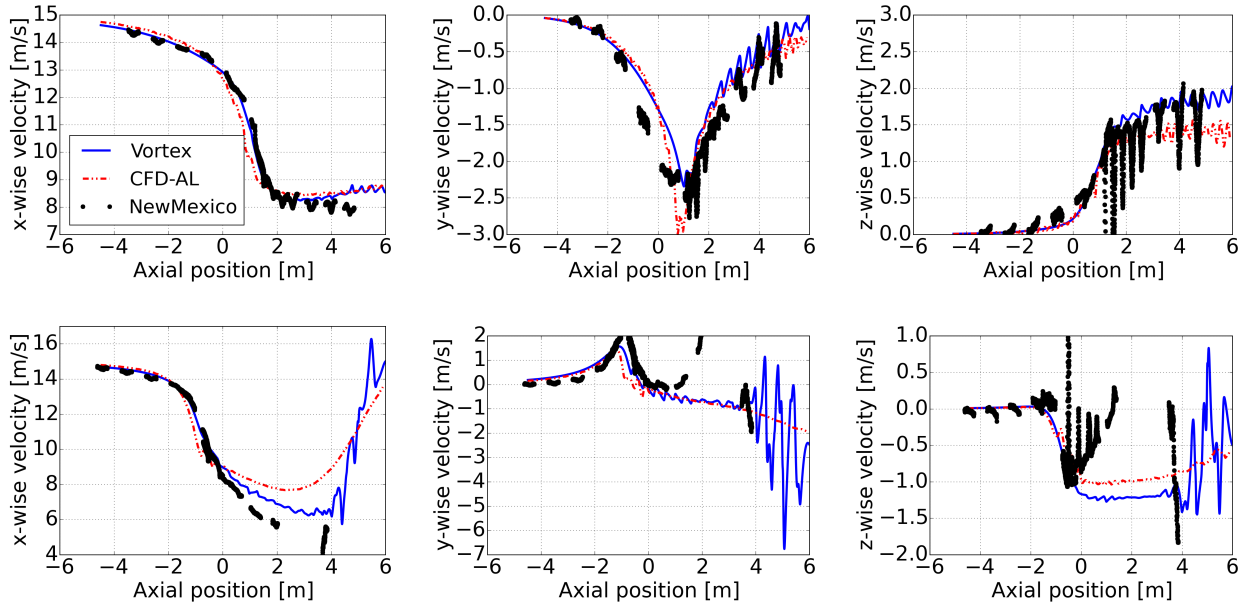


Figure 5: Yawed flow - Comparison of instantaneous axial traverse velocities: $y = -1.5m$ (top) and $y = +1.5m$ (bottom) traverses.

flow test case, a very good match has been obtained between vortex calculations and measurements regarding the axial traverses, which are taken near the tip of the blade on both sides of the wind turbine (see Figures 5 and 6). The traverses being aligned with the wind tunnel coordinate system, a strong velocity recovery is observed at positive radial position $y = +1.5$m: the traverse is crossing the wake, which tends to deviate from the “axial" wind tunnel coordinate system, as shown on Figure 6. At the same negative radial position, the wake is deviating towards negative $y$ values, and thus the PIV traverse is fully located into the wake. This phenomenon can be easily observed on Figure 6, which shows an instantaneous snapshot of the axial velocity component in the wake of the wind turbine, together with the location of the axial PIV traverses. Regarding the radial traverses (Figure 7), agreement between the vortex solver, the CFD-AL solver and measurements is excellent. The flow asymmetry is well predicted, and the tip vortices on both upwind and downwind side of the rotor are well resolved. The absence of the hub is clearly visible on the traverses, which cover the entire rotor: an high velocity zone appears around radial station $r = 0$m, with axial velocities greater than

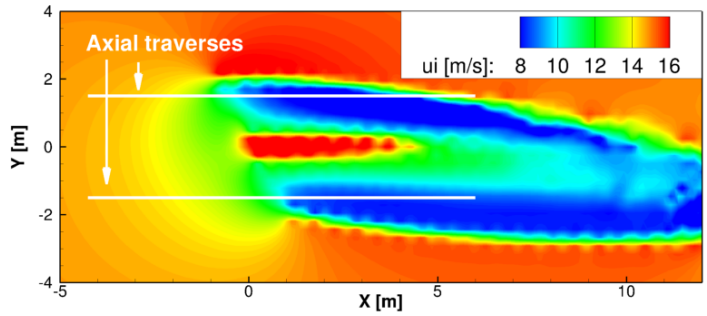


Figure 6: Yawed flow - instantaneous contours of the axial velocity at hub height with location of the axial PIV traverses (vortex solver result).

the infinite wind velocity. This is probably due to some virtually convergent geometry induced by the expansion of the root vortices, also visible on Figure 6. The asymmetry of the flow is visible on the downstream axial velocity calculation and measurements. The axial velocity is lower at negative than at positive radial stations, the blade is advancing, thus relative velocities are higher, and so do the induced velocities.

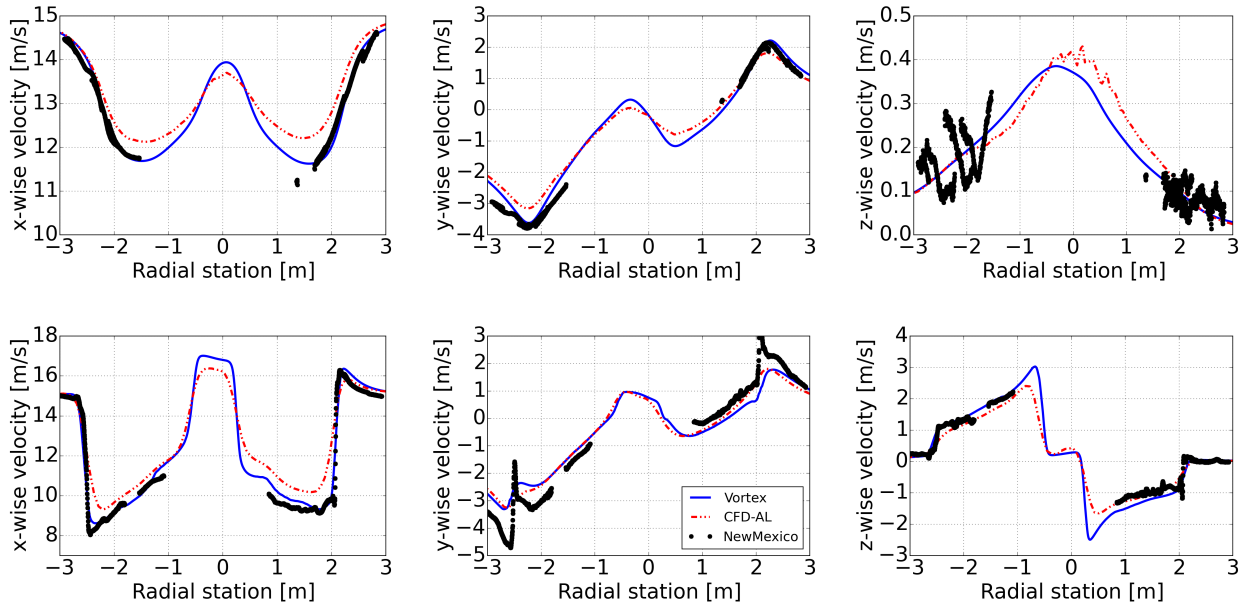


Figure 7: Comparison of radial traverse averaged velocities upstream (top) and downstream (bottom) of the rotor blades.

# 5 Conclusion

From the perspective to select a model well suited for the aero-hydro-servo-elastic analysis of floating wind turbines, possibly interacting, such as multi-turbine concepts, an in-house vortex model and an open-source CFD-AL model have been compared with experimental data. In the same time, a BEM model, well suited for single HAWT configurations but not for multiple turbines, has been improved: the Øye dynamic-stall has been extended to reduce the uncertainty on the input data and, most importantly, a new yaw model has been proposed, with a clear improvement when compared

with the standard Glauert model, keeping the number of constant parameters very low when compared with existing models. Globally, the vortex solver predictions were closer to the experiment than the CFD-AL model, which is probably due to the low dissipation of the model. The computational time is also more attractive, thanks to a GPU parallelisation.

## Acknowledments

NewMexico data used have been supplied by the consortium which carried out the EU FP5 project MEXICO: “Model rotor EXperiments In COntrolled conditions".

## References

[1] F. Blondel, R. Boisard, M. Milekovic, G. Ferrer, C. Lienard, D.Teixeira, Validation and Comparison of Aerodynamic Modelling Approaches for Wind Turbines, Journal of Physics: Conference Series 753 022029, 2016.

[2] K. Boorsma, J.G. Schepers, New MEXICO experiment, Preliminary overview with initial validation, ECN report ECN-E–14-048, 2014.

[3] T. Chaviaropoulos, H.-J. Kooijman, J. Madsen, G. Schepers, N. Sorensen, M. Stettner, AVATAR Deliverable D1.1 Reference Blade Specification, AVATAR project deliverable, 2014.

[4] M. Churchfield, S. Lee, P. Moriarty, Overview of the simulator for wind farm application (SOWFA). NREL Presentation, 2014.

[5] H. Glauert, Airplane Propellers, Springer Berlin, 1935.

[6] H. Hand, D. Simms, L. Fingersh, D. Jager, J. Cotrell, S. Schreck, S. Larwood, Unsteady Aerodynamics Experiment Phase VI: Wind Tunnel Test Con gurations and Available Data Campaingns, NREL/TP-500-29955, 2001.

[7] M. H. Hansen, M. Gaunaa, H. H.A. Madsen, A Beddoes-Leishman type dynamic stall model in state-space and indicial formulations, Risøreport No. 1354, 2004.

[8] J. Katz, A. Plotkin, Low-Speed Aerodynamics, 2nd ed., Cambridge University Press, 2001.

[9] C. Le Cunff, J.M. Heurtier, L. Piriou, C. Berhault, T. Perdrizet, D. Teixeira, G. Ferrer, J.C. Gilloteaux, Fully Coupled Floating Wind Turbine Simulator Based on Nonlinear Finite Element Method: Part I-Methodology, ASME2013 32nd International Conference on Ocean, Offshore and Arctic Engineering, Vol. 8.

[10] S.A. Ning, G. Hayman, R. Damiani, J. Jonkman, Development and Validation of a New Blade Element Momentum Skewed-Wake Model within AeroDyn, AIAA Science and Technology Forum and Exposition 2015, January 5–9 (preprint), 2015.

[11] S. Øye, Dynamic Stall Simulated as Time Lag of Separation, Technical Report, Technical University of Denmark, 1991.

[12] A. Robertson et al., Offshore Code Comparion Collaboration Continuation Within IAE Wind Task 30: Phase II Results Regarding a Floating Semisubmersible Wind System (Preprint), 33rd International Conference on Ocean, Offshore and Arctic Engineering, NREL/CP-5000-61154, 2014.

[13] S. Sarmast, W.Z. Shen, W.J. Zhu, R.F. Mikkelsen, S.P. Breton, S. Ivanell, Validation of the actuator line and disc techniques using the New MEXICO measurements, Journal of Physics: Conference Series 753 032026, 2016.

[14] J.G. Schepers, Engineering Models in Wind Energy Aerodynamics, Development, Implementation and Analysis using Dedicated Aerodynamic Measurements, PhD Thesis, Netherlands, 2012.

[15] J. Weissinger, The Lift Distribution of Swept-Back Wings, NACA Technical Memorandum N. 1120, 1947.

# A Surface plots of the normal forces in yaw

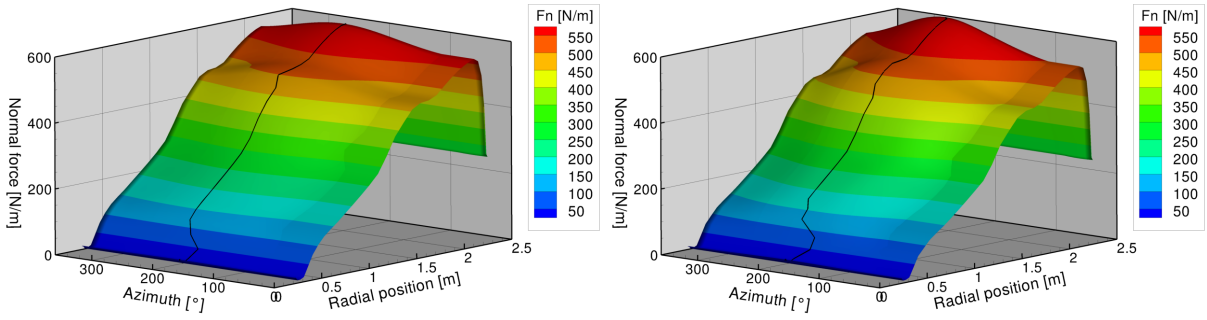


Figure 8: Yawed flow - Surface plot of the normal force against radial position and azimuth, black line indicating the maximum of the normal force at each radial position. $U_\infty \approx 18m/s$, $\Psi \approx 8°$ (left), $U_\infty \approx 15m/s$, $\Psi \approx 15°$ (right).

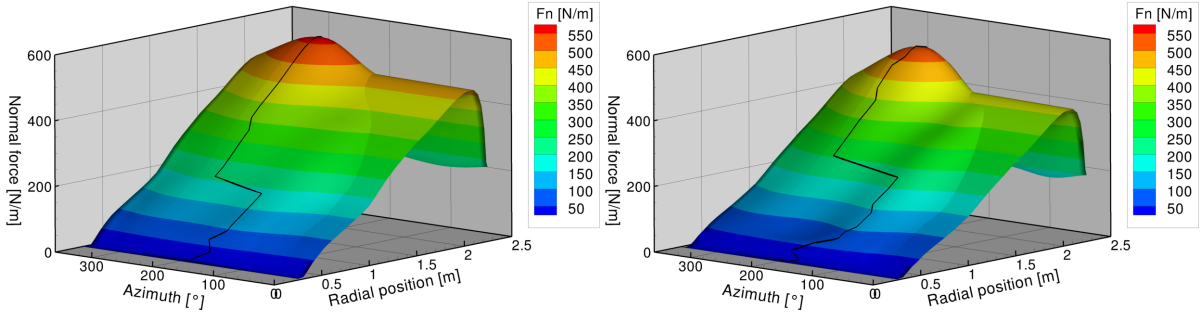


Figure 9: Yawed flow - Surface plot of the normal force against radial position and azimuth, black line indicating the maximum of the normal force at each radial position, $U_\infty \approx 15m/s$, $\Psi \approx 30°$ (left), $U_\infty \approx 15m/s$, $\Psi \approx 45°$ (right).

# B Supplementary validation cases for the new yaw model

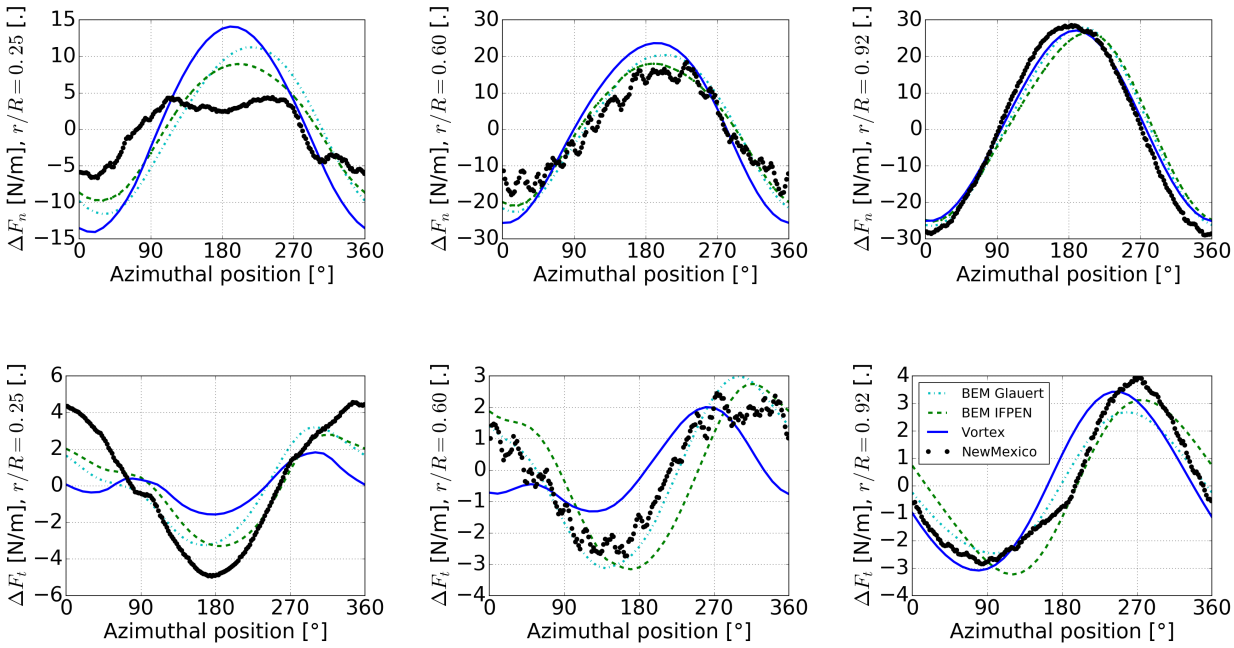


Figure 10: Yawed flow - Variation of the normal (up) and tangential (down) forces around the mean value near the root (left), near mid-span (center) and near the tip (right). $U_\infty \approx 18m/s$, $\Psi \approx 8°$.

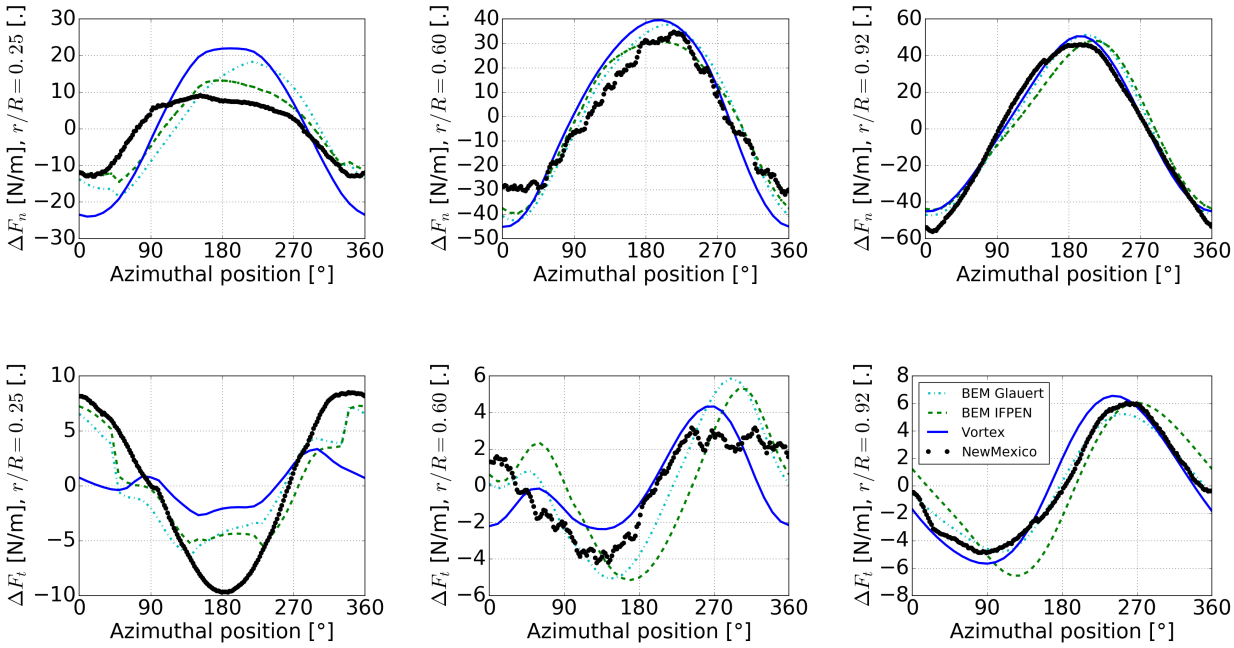


Figure 11: Yawed flow - Variation of the normal (up) and tangential (down) forces around the mean value near the root (left), near mid-span (center) and near the tip (right). $U_\infty \approx 18m/s$, $\Psi \approx 15°$.

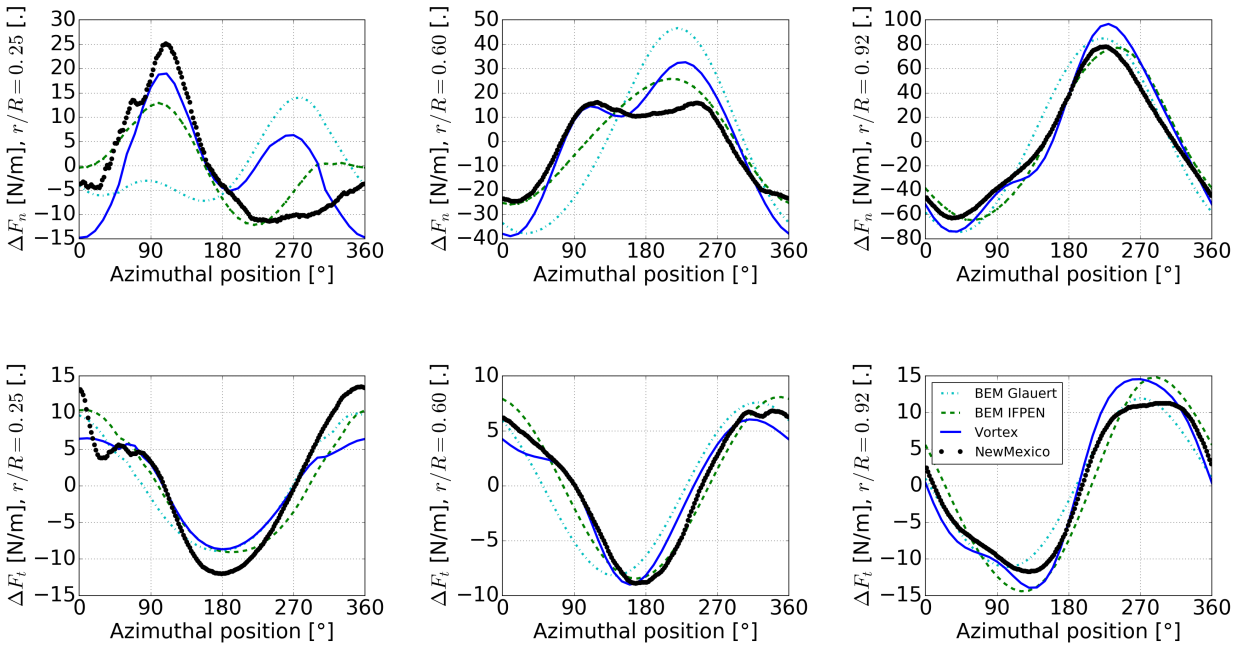


Figure 12: Yawed flow - Variation of the normal (up) and tangential (down) forces around the mean value near the root (left), near mid-span (center) and near the tip (right). $U_\infty \approx 15m/s$, $\Psi \approx 45°$.

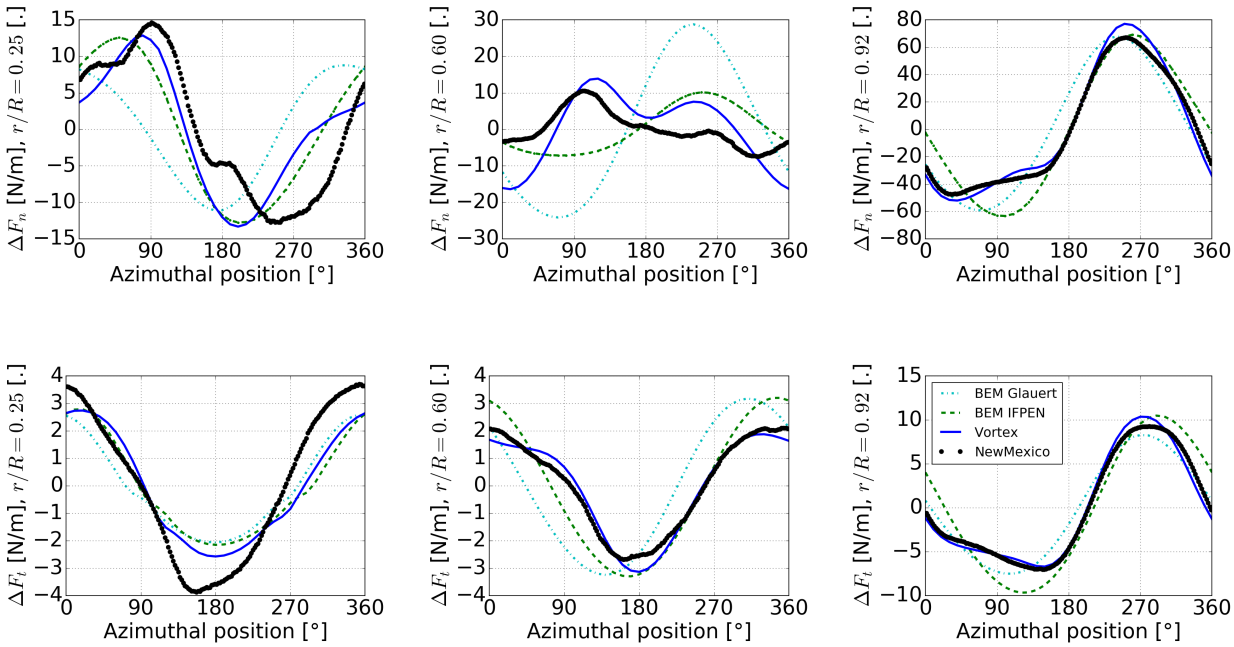


Figure 13: Yawed flow - Variation of the normal (up) and tangential (down) forces around the mean value near the root (left), near mid-span (center) and near the tip (right). $U_\infty \approx 10m/s$, $\Psi \approx 45°$.